INSTITUTE OF PHYSICS PUBLISHING and INTERNATIONAL ATOMIC ENERGY AGENCY NUCLEAR FUSION

Nucl. Fusion **43** (2003) 1693–1709 PII: S0029-5515(03)67272-8

Fusion energy with lasers, direct drive targets, and dry wall chambers

J.D. Sethian[1], M. Friedman[1], R.H. Lehmberg[1], M. Myers[1], S.P. Obenschain[1], J. Giuliani[1], P. Kepple[1], A.J. Schmitt[1], D. Colombant[1], J. Gardner[1], F. Hegeler[2], M. Wolford[3], S.B. Swanekamp[4], D. Weidenheimer[5], D. Welch[6], D. Rose[6], S. Payne[7], C. Bibeau[7], A. Baraymian[7], R. Beach[7], K. Schaffers[7], B. Freitas[7], K. Skulina[7], W. Meier[7], J. Latkowski[7], L.J. Perkins[7], D. Goodin[8], R. Petzoldt[8], E. Stephens[8], F. Najmabadi[9], M. Tillack[9], R. Raffray[9], Z. Dragojlovic[9], D. Haynes[10], R. Peterson[10], G. Kulcinski[10], J. Hoffer[11], D. Geller[11], D. Schroen[12], J. Streit[12], C. Olson[13], T. Tanaka[13], T. Renk[13], G. Rochau[13], L. Snead[14], N. Ghoneim[15] and G. Lucas[16]

[1] Plasma Physics Division, Naval Research Laboratory, Washington, DC, USA
[2] Commonwealth Technology, Inc. Alexandria, VA, USA
[3] SAIC, McLean, VA, USA
[4] JAYCOR, Alexandria, VA, USA
[5] Titan Pulse Sciences Division, San Leandro, CA, USA
[6] Mission Research Corporation, Albuquerque, NM, USA
[7] Lawrence Livermore National Laboratory, Livermore, CA, USA
[8] General Atomics, San Diego, CA, USA
[9] University of California, San Diego, CA, USA
[10] University of Wisconsin, Madison, WI, USA
[11] Los Alamos National Laboratory, Los Alamos, NM, USA
[12] Schafer Corp., Albuquerque, NM, USA
[13] Sandia National Laboratories, Albuquerque, NM, USA
[14] Oak Ridge National Laboratory, Oak Ridge, TN, USA
[15] University of California Los Angeles, Los Angeles, CA, USA
[16] University of Santa Barbara, Santa Barbara, CA, USA

E-mail: sethian@this.nrl.navy.mil

Received 14 October 2002, accepted for publication 22 July 2003
Published 1 December 2003
Online at stacks.iop.org/NF/43/1693

Abstract
A coordinated, focused effort is underway to develop Laser Inertial Fusion Energy. The key components are developed in concert with one another and the science and engineering issues are addressed concurrently. Recent advances include: target designs have been evaluated that show it could be possible to achieve the high gains (>100) needed for a practical fusion system.These designs feature a low-density CH foam that is wicked with solid DT and over-coated with a thin high-Z layer. These results have been verified with three independent one-dimensional codes, and are now being evaluated with two- and three-dimensional codes. Two types of lasers are under development: Krypton Fluoride (KrF) gas lasers and Diode Pumped Solid State Lasers (DPSSL). Both have recently achieved repetitive 'first light', and both have made progress in meeting the fusion energy requirements for durability, efficiency, and cost. This paper also presents the advances in development of chamber operating windows (target survival plus no wall erosion), final optics (aluminium at grazing incidence has high reflectivity and exceeds the required laser damage threshold), target fabrication (demonstration of smooth DT ice layers grown over foams, batch production of foam shells, and appropriate high-Z overcoats), and target injection (new facility for target injection and tracking studies).

PACS numbers: 52.57.-z, 42.55.Xi, 42.55.Lt, 52.57.Bc, 83.60.-a, 52.57.Fg, 52.59.Mv

1. Introduction

We are carrying out a coordinated, focused research programme to develop Laser Inertial Fusion Energy (Laser IFE). The approach is based on lasers, direct drive targets, and dry wall chambers. The key components are developed in concert with one another and the science and technology are addressed at the same time. This integrated approach ensures Laser Fusion Energy will be developed as a coherent system.

The attractiveness of this approach lies in its inherent simplicity, its separable architecture, and the modular nature of the laser driver. The targets are spherical shells, which can be fabricated in droplet generators, and thus naturally lend themselves to mass production. None of the target components (except tritium) need to be recycled. The first wall is a passive structure that does not have to hold vacuum. This allows the wall to be made in individual sectors that can be replaced during the plant lifetime. It also allows more choices for the first wall material, such as advanced composites that may have radiological advantages. The separable nature of the power plant allows the principal components to be developed separately before being integrated into the system. Just as importantly, it allows economical upgrades as new technologies are developed. The laser is modular, and would consist of many (about 60) identical beam lines. Hence, it is only necessary to develop one of these lines to prove the technology. All of these factors should lead to a faster, lower risk, lower cost path to fusion energy.

Recent advances have been made in all areas of laser fusion energy. Target designs, based on codes that are being benchmarked with experiments, have been developed which have gains of 120–180. Gains >100 are considered sufficient for a fusion power plant. These are one-dimensional calculations [1]. More recent integrated two-dimensional designs show the same performance. Two types of lasers are being developed: Krypton Fluoride (KrF) gas lasers and Diode Pumped Solid State Lasers (DPPSL). Both have achieved repetitively pulsed first light and both are making progress towards meeting the fusion energy requirements for efficiency, durability, and cost. In chamber designs, an operating window has been established for target yield, chamber radius, and chamber gas pressure that will avoid first wall vaporization, allow target injection without compromising the frozen deuterium–tritium (DT) fuel, and operate at reasonable efficiency. However, long-term material behaviour is an open issue. This is being addressed both with experiments that include exposing candidate first wall materials to ions and x-rays at fusion relevant parameters, and in developing new first wall materials. A new chamber dynamics model will allow us to determine how the chamber conditions evolve between shots. In the area of final optics, experiments have shown that a grazing incidence aluminium mirror is both highly reflective ($>98\%$) and can exceed the required laser damage threshold of $5\,\mathrm{J\,cm^{-2}}$. In target fabrication, methods have been developed to apply an Au–Pd alloy coating outside the target that will meet the requirements for the target physics, DT permeation times, and the high IR reflectivity needed to help the target survive as it traverses the hot chamber. Divinyl benzene foam shells of proper dimensions and density have been produced on a batch basis that lends itself to mass production. These shells can meet the requirements for low oxygen content, mechanical strength, and straightforward over-coating. The cost of fabricating and injecting these targets on a mass production basis has been estimated to be \$0.16 each. This analysis was based on a chemical engineering analysis of all the process steps and assuming a commercial process plant environment. Recently, it has been demonstrated that ultra-smooth DT ice layers can be grown over a foam underlay, and that these ice layers remain sufficiently smooth at low temperatures. This aids target survival during injection into the chamber. A facility to accelerate, inject, and track targets is nearing completion.

The work cited in this paper leverages off the wide body of target physics research and target fabrication development carried out in the US Inertial Confinement Fusion (ICF) programme. In particular, studies at the Naval Research Laboratory [2, 3] and the University of Rochester [4–6] have been dedicated at investigating the physics and technology of direct drive targets. Results of that research have directly benefited the work discussed here.

2. High gain target design

A typical high gain target direct drive design is shown in figure 1.

The current designs share several common features:

1. The laser pulse has a low intensity 'foot' followed by a rise to maximum intensity. In some cases a single intense 'picket' pulse precedes the foot.
2. The ablator is composed of a low-density foam with DT wicked into it. The foam can significantly increase the laser absorption.
3. The design preheats the ablator by some means (shocks, x-rays, or a combination). This raises the isentrope of the ablator, and hence lowers the growth rate of the Rayleigh–Taylor instability. In some designs the ablator is preferentially heated, while the fuel remains on a lower isentrope. This increases the stability without substantially reducing gain.
4. The laser is 'zoomed': the spot size is decreased in radius to match the compressing target. This reduces the amount of light lost to refraction and/or absorbed far away from the ablation surface, and thus increases the absorption and coupling efficiency of the design.
5. The designs include a thin high-Z layer (such as Pd) outside the target. This has been shown experimentally to substantially reduce the imprint of laser non-uniformities, and hence mitigates the seeding of hydrodynamic instabilities [7]. This is shown in figure 2.

The first high gain targets [1] used radiation preheating, an incident laser energy of 1.3 MJ, and had energy gains well above 100. In these targets, α, the average isentrope within the fuel region, was slightly greater than 1. (α is the ratio of the total DT pressure to the Fermi-degenerate pressure.) A one-dimensional analysis showed that the Rayleigh–Taylor instability grew less than 6 e-folds (net growth) when averaged over the initial surface roughness spectrum. This corresponds to less than 400 times the initial perturbation amplitude. The high-Z coating was applied to the outside of the ablator to ensure that

it would be blown off before the laser pulse reached high intensities. When it was realized that it was difficult to provide enough preheat with x-rays, the design evolved to rely more on shocks to establish the higher ablator isentrope. The high-Z material was kept for imprint reduction as described above. It was originally chosen to be gold, but was later changed to palladium because the latter's permeability to hydrogen (DT) is important for target fabrication. Based on a number of calculations, any mixture of Au and Pd would allow similar target performance; the only difference being the required thickness of the coating. The predicted one-dimensional gain of these targets, as a function of the Pd layer thickness, is shown in figure 3. The figure shows results from the first generation, 154 MJ target, and a second generation, 400 MJ target.

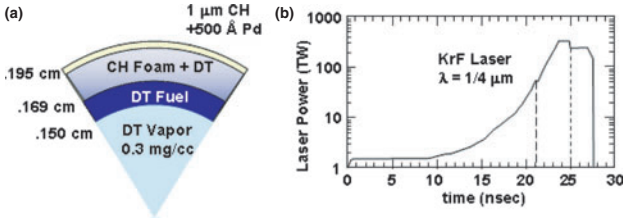

Figure 1. (*a*) Typical NRL high-gain target design. (*b*) Laser pulse shape. Dashed lines are zoom points.

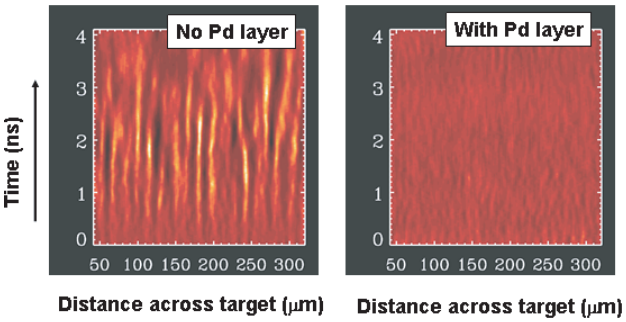

Figure 2. X-ray streak radiographs of ablatively accelerated planar targets show no measurable instability growth with 1200 Å Pd layer on target front surface.

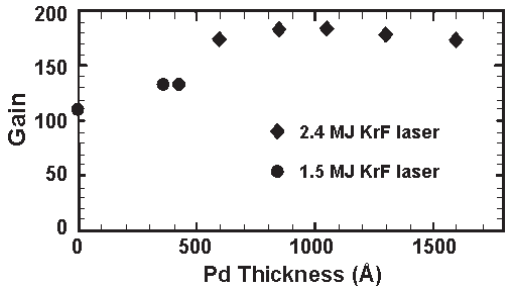

Figure 3. Target gain as a function of Pd thickness.

In a later design, the high-Z material was uniformly mixed with the ablator. The intensity of the foot pulse was the same as required for the $\alpha = 1$ design. In this case, the high-Z material can increase the isentrope of both the ablator and the fuel. Thus, to minimize the fuel preheating, only small amounts of high-Z material were added. With an incident energy of 2.5 MJ (KrF light) and zooming, the gain of the target was predicted to be 163. One-dimensional dispersion relations for this target predict that the single fastest growing mode (near $l = 150$) grew 6.8 e-folds.

Recent one-dimensional calculations show the gain is not affected if the amount of DT vapour inside the target is lower than that shown in figure 1(*a*). In fact, there is no need for any vapour at all. This allows operation at lower target temperatures, which, as discussed in section 8, benefits target injection.

Currently, the NRL FAST series of codes is being used to evaluate these targets with high-resolution two-dimensional fully integrated simulations. These resolve all the wavelengths relevant to the hydrodynamic instability. All known sources of non-uniformity are accounted for: inner and outer surface roughnesses (based on NIF pellet specifications), laser imprint from modelling of the optical smoothing, either by ISI—Induced Spatial Incoherence, or SSD—Smoothing by Spectral Dispersion, and low-mode laser pointing and power imbalances (based on modelling from the NIF laser system). Simulations are ongoing for the NIF baseline target design, and are beginning for the NRL-designed high-gain KrF-driven targets. An example calculation is shown in figure 4. More recent results show the two-dimensional gains for an IFE target driven by a 2.5 MJ laser to be the same as the one-dimensional gains described above. In those calculations the power balance around the target (irradiation non-uniformity) is assumed to be perfect, the outer surface of the target is assumed to have a roughness of 0.125 μm RMS, the inner surface has a roughness of 1.0 μm RMS, the laser has a bandwidth of 1 THz with ISI smoothing, and a picket is applied.

Two-dimensional single mode calculations for a 400 MJ target design have also been carried out with LASNEX. This target is slightly larger than that shown in figure 1, and has a 6 μm thick pure CH outer layer. The calculations show that the stability is enhanced by adding a single high-intensity spike, or 'picket' early in the foot of the laser pulse. The prepulse shock heats the ablator to a higher

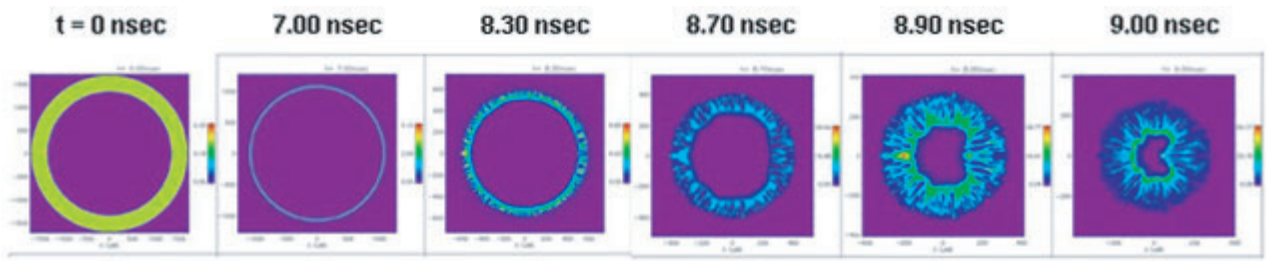

Figure 4. Two-dimensional simulations showing density during an NIF pellet implosion.

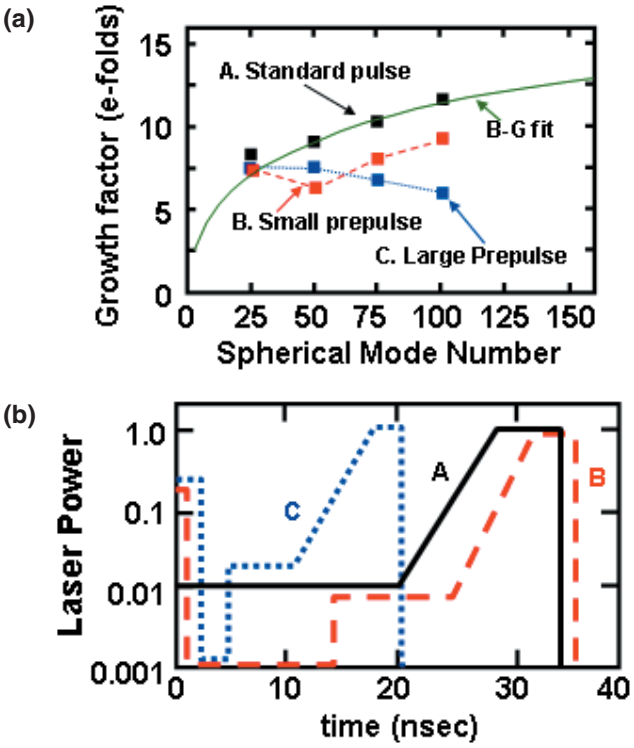

Figure 5. (*a*) Single mode e-folds versus spherical mode number for the (*b*) pulse shapes shown at right.

isentrope (with a concurrent reduction in Rayleigh–Taylor growth) but decays before reaching the fuel. This idea, including experiments, has been explored independently by the University of Rochester [8].

In these LASNEX calculations particular attention was paid to reduce the numerical noise inherent in laser energy deposition when modelling two-dimensional growth rates. It is now possible to perform full, time-dependent implosions to ignition with two-dimensional laser ray-trace in operation from time zero. Numerical noise growth amplitudes at the fuel/ablator interface at ignition have been reduced to $\sim 10^{-11}$–10^{-10} cm, which is comparable to indirect-drive targets driven by a uniform x-ray source.

Figure 5 shows plots of the single mode growth factors (e-folds) versus spherical mode number, $l = \pi r(t)/\lambda(t)$, for three different pulse shapes. Pulse shape A is the 'conventional' pulse: foot plus main drive, Pulse shapes B and C have a small and large prepulse, respectively. At spherical mode numbers around $l \sim 75$–100, growth factors have been reduced from ~10.5 (standard pulse shape) to ~6.5 e-folds (large prepulse). These are comparable to the growth factors seen for indirect drive heavy-ion targets. As shown in figure 5, the two-dimensional growth factors are in good agreement with the semi-analytic Betti–Goncharov one-dimensional model [9] plus Bell–Plesset convergence.

The impact of these growth factors on late-time shell breakup has been assessed by application of the non-linear multimode saturation model of Haan [10]. For comparison with earlier work an initial roughness spectrum based on NIF specifications was used. The results are summarized in table 1. The late-time shell breakup (the peak-to-valley bubble amplitude divided by the shell thickness) has been reduced from ~80% to an acceptable 21% with virtually no penalty in gain. This is consistent with the two-dimensional FAST modelling described above. Note that the breakup can be reduced to a negligible 2%, with a gain that is still high enough for fusion energy. However, the small prepulse case should be more than adequate.

Table 1. Effects of shaped pulse on target performance.

Pulse shape (see figure 5(*b*))	Laser (MJ)	Yield (MJ)	Gain	Maximum shell breakup (%)
A (standard)	2.4	430	180	83
B (small prepulse spike)	2.5	420	170	21
C (large prepulse spike)	3.1	360	110	2

3. KrF laser

KrF lasers are gas lasers that are pumped by electron beams, and lase at 248 nm. Development is being carried out with the Electra Programme at NRL. The key components under development are: an efficient and durable pulsed power system, a durable electron beam emitter (cathode), a long life, high transmission foil support structure (hibachi), a recirculator to cool and quiet the laser gas, and long-life optical windows [11]. Electra should produce 500–800 J in 100 ns when run as an amplifier. The technologies will be directly scalable to a fusion power plant sized laser beam line. The Electra laser facility is shown in figure 6. A first generation pulsed power system has been built to develop the laser components. The system produces two 500 keV, 100 kA, 100 ns electron beams, each with a cross-section 30 cm high by 100 cm wide. The pulsed power system can run at 5 Hz for 5 h (100 000 shots). Ten-thousand shot e-beam runs (10 kW) are commonplace. The system has run as a laser oscillator, and in early tests has produced 500 J of laser light per pulse in 10 shot bursts.

3.1. Advanced pulsed power

An all-new solid-state, laser-triggered switch has been developed that will become the basis for a pulsed power system that can meet the IFE requirements for rep-rate, efficiency, durability, and cost. The switch uses a four-junction silicon device that is optically triggered by two diode lasers. The lasers flood the entire switch volume with photons, whose energy is just above the band edge of the silicon. This gives switching times of the order of 100 ns, or more than 10 times faster than other solid-state switches. The lasers are kept on during the entire electrical pulse to increase the system efficiency. Using a four-junction device enables operation at voltages of 20 kV. We call this device a *Laser Gated and Pumped Thyristor*. For the first tests, an off-the-shelf Thyristor was modified to accommodate a single diode laser and the necessary optical coupling. The switch operated at 3.2 kV for 10^5 shots at 5 Hz. The current density was 2.7 kA cm^{-2} (121% of the IFE requirement) and the current rate of rise was 1.4×10^{10} A s^{-1} cm^{-2} (154% of the IFE requirement). A second generation switch has been built that uses advanced, purpose-built construction techniques, and accommodates the

two-sided pumping. This switch has operated at 15.2 kV, held 24 kV in a pulse charge, and is now undergoing durability tests.

3.2. Hibachi (foil support structure)

A hibachi concept has been developed that demonstrates an energy deposition transmission efficiency of up to 75% on Electra (500 keV), with the potential to go to greater than 80% at full system operating voltages (750 keV). The energy deposition efficiency is defined as the ratio of the energy deposited in the laser gas divided by the energy in the diode. The high transmission efficiency was achieved with two innovations: (1) eliminating the anode foil on the diode side of the hibachi structure, and (2) patterning the electron emitter into strips so that the beam 'misses' the hibachi ribs. While conceptually simple, these are difficult in practice: the beam strips spread due to the highly non-uniform electric fields caused by eliminating the anode, and the beam rotates and shears due to combined applied and self-magnetic fields. These effects are eliminated by narrowing and 'counter-rotating' the emitters so that the beam 'strips' propagate parallel to the ribs when they get to the hibachi. This concept is shown in figure 7. As a bonus, patterning the beam into strips also delays and reduces the 'transit time' instability that is characteristic of large area electron beams [12].

While the topology of the cathode strips can be determined empirically, this does not give the predictive capability needed to design larger systems. This is a rather complex phenomenon to model and requires a full three-dimensional PIC simulation of the exact experimental geometry, including the rib structure,

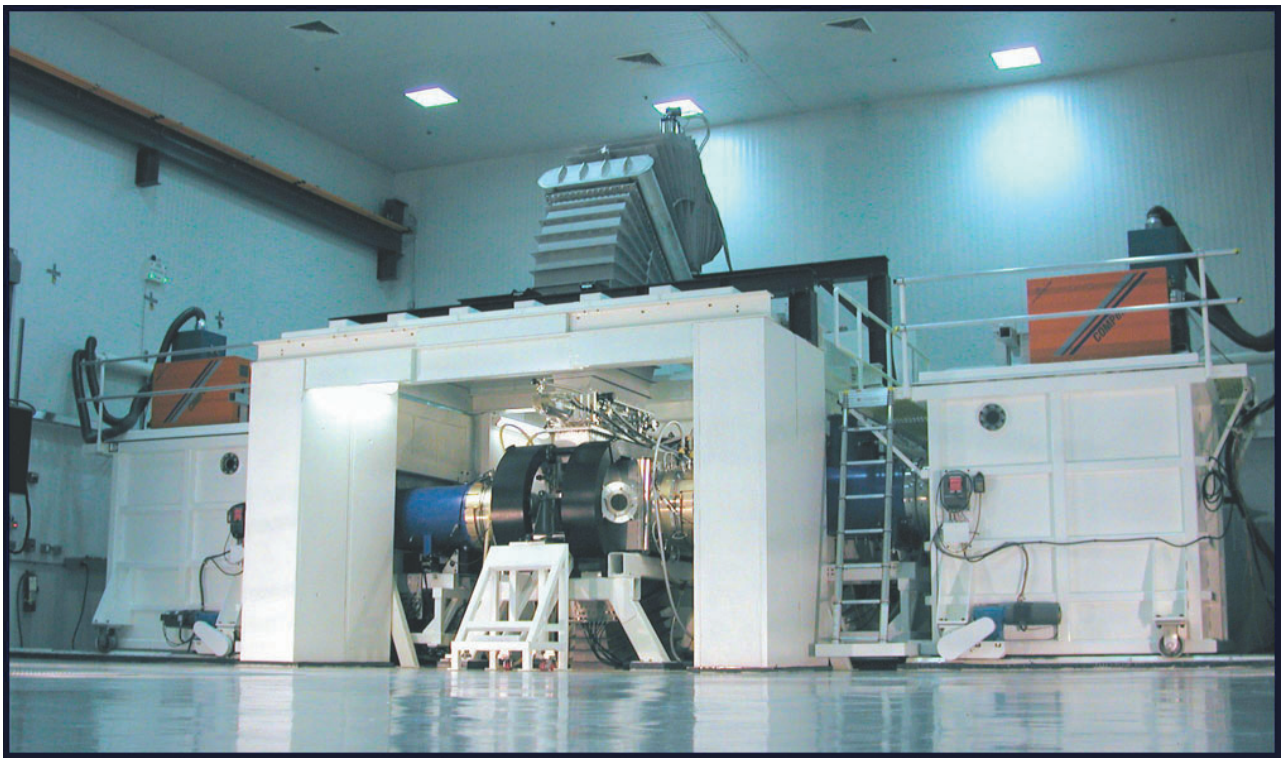

Figure 6. The Electra Laser Facility. Electra has repetitively produced 500 J per pulse of laser light.

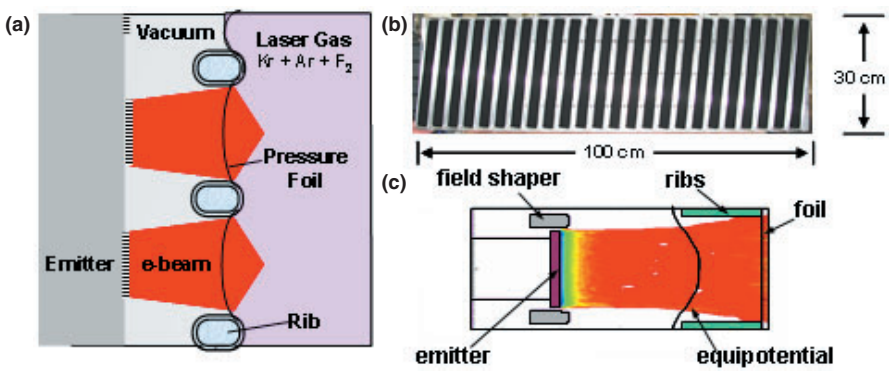

Figure 7. (*a*) Drawing of hibachi concept. (*b*) Photo of cathode showing the counter-rotated emitter strips. (*c*) LSP modelling of beam propagation past ribs.

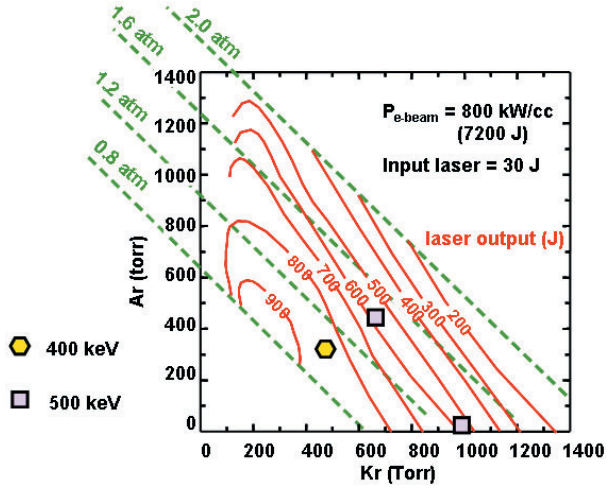

Figure 8. Orestes Code predictions for Electra main amplifier for two different e-beam energies.

laser gas, and magnetic field. This was achieved by running the Large Scale Plasma (LSP) code, developed by MRC, Albuquerque, on NRL's parallel processors. The simulations accurately predict both the cathode counter rotation angle and the energy deposition efficiency. A simulation of a beam 'strip' is also shown in figure 7.

3.3. KrF physics code development

The 'Orestes' KrF Physics code has been developed to both predict the behaviour of Electra and to serve as a tool to design full-scale (30–100 kJ) systems. Orestes follows 122 reactions with 24 species and has been benchmarked against a wide range of KrF experiments under different conditions. Using experimentally determined energy depositions, Orestes predicts the output for Electra to be between 550 and 850 J, depending on the experimental conditions. See figure 8.

3.4. KrF amplifier windows

The amplifier windows, which are typically UV grade fused silica, need to have an index matching dielectric coating to minimize transmission losses. The coatings operate in a hostile environment—intense laser light, fluorine, UV, x-rays, electrons, and, if there is even trace water present, HF. The development of the coatings is ongoing; however, good fluorine laser resistance with high transmission has been obtained with a MgF/Alumina/MgF dielectric stack.

4. Diode pumped solid state laser

Diode Pumped Solid State Laser (wavelength 351 nm) development is being carried out with the Mercury Program at LLNL. The ultimate goal is to produce a 100 J, 10 ns, 10 Hz, 10% efficient laser. Like the Electra KrF laser, the technologies developed on Mercury are scalable to a full-size power plant laser [13]. To achieve the goals of Mercury, three key technologies needed to be developed: high-peak-power diode arrays [14], $Yb^{3+}:Sr_5(PO_4)_3F$ (Yb : S-FAP) crystalline gain slabs [15], and helium gas cooling of the gain media [16]. A picture of the facility is shown in figure 9.

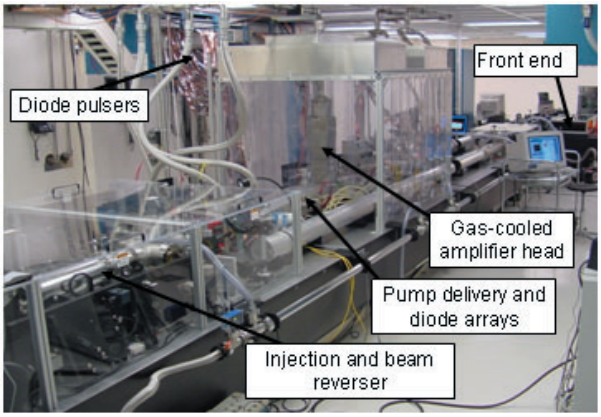

Figure 9. The mercury laser with a single amplifier head produces up to 34 J of energy per pulse.

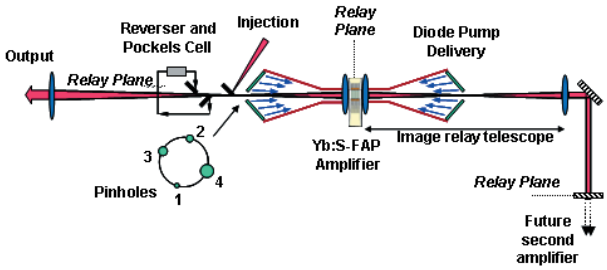

Figure 10. Schematic of the Mercury Laser.

The system is schematically illustrated in figure 10. Light from the diode array is guided to the amplifier slabs through multiple reflections within a hollow lens duct and homogenizer. The Yb : S-FAP amplifier slabs are potted into aerodynamic vanes, which are cooled by helium gas flowing at Mach 0.1. By means of angular multiplexing, the beam is injected into the main cavity and relay-imaged two times through the amplifier head. The beam is then re-injected via a U-turn loop (called a 'reverser'), which contains a birefringence-compensated Pockels cell [17] (used for ghost and parasitic beam suppression). This allows the beam to pass through the amplifier two more times. A device for 'spectral-sculpting' the input beam, so as to maximize the output bandwidth for beam smoothing, has been developed [18]. To date, one amplifier head has been activated and the system has generated 23 J at 5 Hz for 6×10^3 shots (20 min).

Improvements have been made in the growth of the ytterbium-doped strontium fluorapatite (Yb : S-FAP) crystals. These Czochralski-grown crystals were initially plagued by a number of growth-related defects [19]. However, the defects have been controlled with newly developed procedures including water cutting, acidic polishing, and diffusion bonding. The lifetime and durability of this material is expected to meet the IFE requirements, but will be evaluated experimentally on Mercury.

In the Mercury system, four diode arrays have been activated with each delivering 80 kW of peak power in a 750 μs pulse. An overall transfer efficiency of 83% through the pump delivery system was achieved, and the pump homogeneity matches the ray-trace models. A birefringence-compensated average power KD*P Pockels cell was fabricated and meets

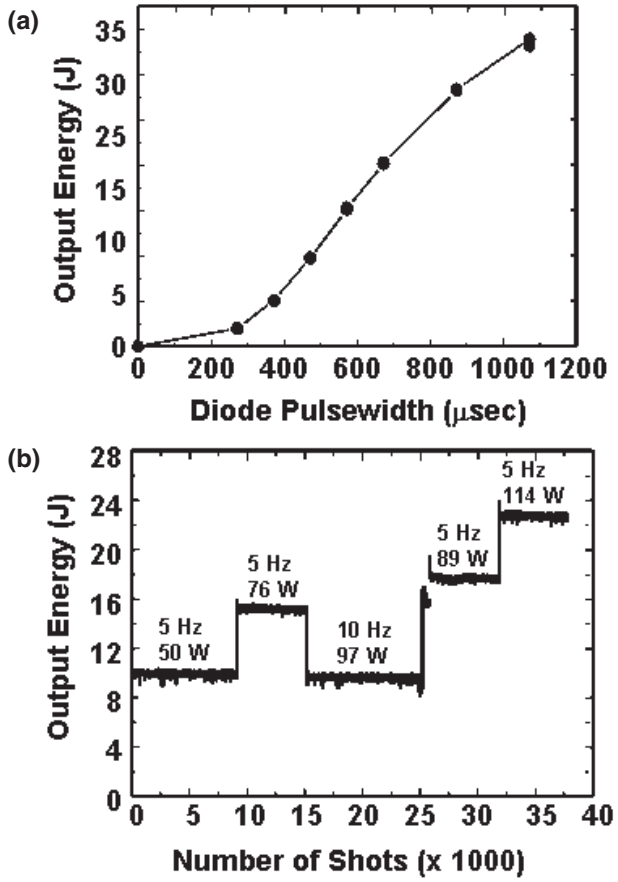

Figure 11. (*a*) Single shot laser energy. (*b*) Operations plot showing output energy and stability for various repetition rates.

the 200 : 1 extinction requirement at 100 W average power. All seven $4 \times 6\,\mathrm{cm}^2$ Yb : S-FAP slabs are currently installed in the amplifier. An example of performance results for one amplifier head appears in figure 11. Up to 34 J has been achieved and reliable operation at 23 J per pulse (20 ns) is plotted below.

5. Chamber development

The explosion of the target, which produces bursts of neutrons, gammas, x-rays and charged particles, is the central event in inertial fusion. Everything that happens before the explosion (laser operation, focusing optics, target fabrication and injection, laser–plasma interactions, and implosion) causes this event to occur. Everything that happens after the explosion (chamber protection, energy conversion, chamber recovery, activation, and balance of plant) is influenced by the target explosion. The development of a successful chamber depends on two issues:

1. Can an operating window be established in which a set of chamber parameters (radius, materials, wall temperature, and environment) simultaneously allows distortion-free propagation of the laser beams, successful injection of the target, survival of the first wall, and high thermal efficiency?
2. Can the chamber recover to this state to allow successful target injection and laser beam propagation on the next shot?

5.1. Operating windows

Establishing the operating window for an IFE chamber is a complex process that involves balancing several factors. The target produces a 'threat spectrum' of neutrons, x-rays, and charged particles. These propagate with different velocities and hence hit the chamber wall at different times. The first wall response depends on when these hit the wall, the energy they impart to the wall, and the wall material. In some designs the chamber is filled with Xe gas. The Xe absorbs energy from the ions (and to a lesser extent, the x-rays) and then re-radiates it on a longer timescale, as determined by the opacity and emission of the Xe. This stretches out the energy deposition on the wall and allows thermal conduction to keep the material below the temperature at which damage will occur. There are upper limits to the allowable gas density, however, as the background gas affects laser propagation, target tracking, and target survival.

5.1.1. Threat spectrum calculation. The threat spectra produced by the targets shown in figure 3 have been calculated using both LASNEX [20] and the one-dimensional Lagrangian radiative hydrodynamics code BUCKY [21]. Both codes predict the same gains as the NRL FAST Code. They predict similar threat spectra for both the low yield 154 MJ and high yield 400 MJ targets. About 1–2% of their output is in x-rays. Half of the photons have energy above 30 keV. Charged particles ('burn ions') comprise 13–14% of the target output, and 'debris ions' comprise 15–16%. The latter are moving considerably slower, allowing time of flight spreading to greatly mitigate the total threat to the wall. The balance of the energy release is, of course, in neutrons. An example of this energy partitioning (from BUCKY) is shown in figure 12.

5.1.2. First wall material choices. Development of the first wall for an IFE chamber faces many of the same challenges as for magnetic fusion energy (MFE). For both approaches thermodynamic efficiency is important. This tends to favour higher operating temperatures. For both systems a driving concern is the environmental acceptability of the power plant. Thus, both approaches call for low-activation materials. And for both approaches the time averaged energy flux to the wall are about the same. The loading on an IFE chamber wall has many of the same characteristics (frequency, particle flux, affected area, base temperature) as an ITER Type 1 ELM mode [22]. As a result of these considerations, the two current leading candidates for the chamber first wall material are similar to those for MFE: a carbon fibre composite, as in the SOMBRERO study [23, 24], and tungsten. The selection is based on both high thermal conductivity and high sublimation (C) or melting (W) temperatures.

(Although there are similarities between the IFE and MFE wall loading, the specific loading is substantially higher due to the pulsed nature of the IFE system. Specifically, the neutrons, photons, fast ions, and debris ions arrive at the wall within 2.5 μs. This yields an instantaneous heat loading of more

than 10 000 MW m^{-2} as compared to 10 MW m^{-2} for an MFE plant. Similarly, the instantaneous neutron displacement rate in IFE can be 10 displacements per atom per second compared to 10^{-6} for MFE.)

In order to develop the chamber operating windows, it is necessary to use models that predict the material response to the emissions from the target. To benchmark these code predictions, candidate chamber first wall materials have been exposed to ions and x-rays at fusion-relevant fluences and spectra. These were carried out with the Z (single shot x-rays) and RHEPP (repetitively pulsed ions) facilities at Sandia. Table 2 compares the experimental results, theoretical predictions, and anticipated threat for the two high gain targets shown in figure 3.

Note that the measured ablation and roughening thresholds are close to the code predictions. The predicted threat to the wall assumes a chamber radius of 6.5 m radius and no gas in the chamber. The number in parenthesis for the ion threat was obtained by applying a $t^{1/2}$ correction for the pulse width. The ions from RHEPP are produced in ~100 ns, whereas in an IFE chamber they are emitted in a double humped distribution over 2.1 μs. This scaling is only an approximation, as its validity depends on several factors (such as the ratio of the thermal diffusion length to the energy deposition length). The main reason is to demonstrate that both Z and RHEPP are producing relevant threats. From the table, it is clear that x-ray damage is not a problem with either target or wall material. The estimated ion fluence is slightly below the damage threshold for the lower yield target, and slightly above it for the higher yield one. This is why, as discussed below, the chamber needs to be filled with gas and the radius extended to 8.25 m for the higher yield target. Note that the addition of Re to tungsten increases its resistance. (However, the addition of Re brings up radiological issues that must be addressed.) All of these results are obtained with room temperature samples, and the behaviour at IFE relevant wall temperatures will be examined. In addition, the long-term effects of roughening will be investigated. It may turn out that roughening, which is due to repetitive thermo-mechanical stresses, rather than melting, may be the limit.

The data discussed above are taken for a few tens of shots. There is concern that damage may be cumulative and will become apparent only after many cycles. This will be studied with the new repetitive x-ray source XAPPER, which is being installed at LLNL. The source, produced by PLEX LLC, uses a radiofrequency-initiated Z-pinch [25], along with a grazing incidence ellipsoidal optic to deliver high fluences of low-energy (100–500 eV) x-rays to a sample. XAPPER will be used to access very high cycles (up to 10^6 pulses at 10 Hz) of x-rays to study surface effects for optics and wall materials for energy deposition levels lower than apparent threshold levels based upon low-cycle tests and single-shot calculations.

In addition to the above, a laser test facility has been set up at UCSD to investigate long-term material behaviour. The advantage of using a laser is that it can provide a clean, low-cost, repetitive, high-duty-cycle, energy source. At first glance it would appear that a laser, which deposits energy on the surface, would not faithfully duplicate the effects of x-rays and ions, which deposit their energy at different depths. This is true initially, but modelling has shown a 10 ns laser pulse can simulate the proper temperature evolution in the wall as it relaxes. The primary phenomena that lead to mass loss from the wall are sputtering, ion/neutron radiation damage, evolution of the wall temperature, and the chamber environment. The UCSD facility will look at the latter two. Comparison of these tests with those from the x-ray and ion tests will help elucidate the loss mechanism, as well as determine the fidelity of this laser-based approach.

5.1.3. Limitations on chamber gas density. As pointed out above, in some cases, particularly with the high yield target, the chamber will have to be filled with some density of Xe gas. There are three phenomena that determine the upper limits of the chamber gas density. In increasing order of allowable gas pressure, they are: survival during injection, tracking in the chamber, and high-fidelity propagation of the laser.

If there is any gas in the chamber at all, it will be at or above the wall temperature. Thus, this hot gas will warm up the injected cryogenic target through a energy exchange. This heat load is in addition to the radiation heating from the hot wall. As discussed in section 8, the temperature of the outer surface of the frozen DT in the target cannot rise above the triple point of solid DT (19.79 K). As shown in section 7, experiments have shown that smooth DT ice layers can be formed over foam layers at temperatures at least as low as 16 K. Thus, the target outer surface can warm up 3.79 K before the outer surface starts to melt. The allowable heat flux on the target depends on the injection velocity. For example, assuming the target is in the chamber for 16 ms (corresponding to a 6.5 m radius chamber and a 400 m s^{-1} injection velocity), the allowable heat flux on a target starting at 16 K is 1.4 W cm^{-2}. If the chamber wall is at 1000 K (727°C), the radiation heating from the wall alone is about 0.2 W cm^{-2}. Calculations show that, to stay below the 1.4 W cm^{-2} total limit, the gas pressure in the chamber should be below 15 mTorr. This assumes the gas temperature is at the wall temperature, and assumes the target shown in figure 1. If there were a 250 mg cc^{-1} foam coating outside the target to provide additional thermal insulation, these same calculations suggest the gas pressure could be 5–8 times higher. Further details of these temperature rise calculations are given in section 8.

In the case of tracking, the gas density has to be low enough such that aerodynamic forces do not appreciably perturb the target trajectory. The target motion becomes random, and the lateral excursions sufficiently large that it becomes difficult to maintain the $\pm 20\,\mu$m laser pointing accuracy required by target physics. Modelling shows that the upper limit to the gas pressure in this case is about 75 mTorr.

The limit on the gas pressure due to laser considerations was investigated in studies carried out at NRL [26]. The behaviour of an ablatively accelerated planar target was determined as a function of background gas pressures ranging from 10^{-6} Torr to 500 mTorr Xe. The experiments showed no evidence of laser beam breakup, nor changes in the central profiles of the shock breakout from the rear of the target. Also, the plasma profiles remained smooth and symmetric in all cases. Minor qualitative changes were seen in the edges of the shock break-outs at pressures above 200 mTorr, but these are thought to be irrelevant in a spherically illuminated target. Nevertheless, it is clear that laser propagation is not currently the factor that determines the allowable background gas.

5.1.4. Examples of chamber operating windows. Figure 13 gives an operating window for a 154 MJ target. The figure gives the temperature evolution at the wall surface and various depths. The example is for a 3 mm thick Tungsten armour, a chamber radius of 6.5 m, and a first wall starting temperature of 500°C. There is no gas in the chamber. Note the tungsten stays well below the melting temperature of 3410°C.

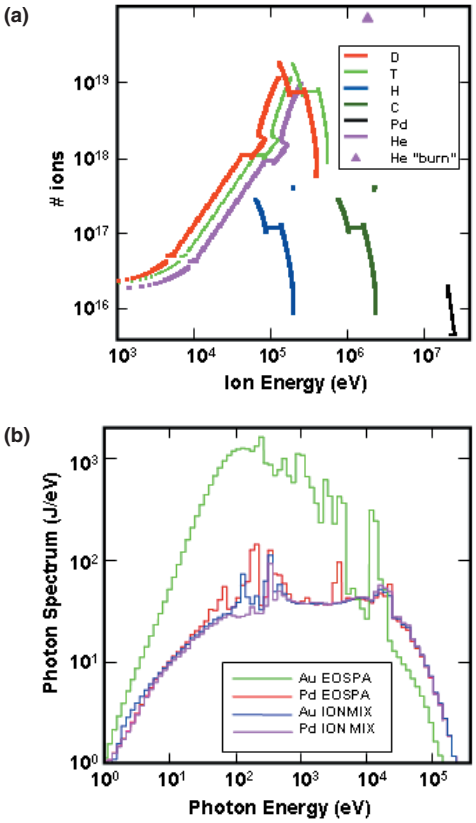

Figure 12. (*a*) Expected time-integrated x-ray spectra emitted by the NRL direct-drive target shown in figure 1. The coating was either 300 Å Au or 1200 Å Pd. Target yields were calculated to range from 300 to 400 MJ. The x-ray spectra were calculated based on two opacity models: EOSOPA (LTE) or IONMIX (Non-LTE). (*b*) Time integrated histogram showing the number of ions per eV. This is for a Pd-coated laser direct-drive target. IONMIX (non-LTE) opacities were used. Note, BUCKY does not presently have mix in the code, which is why some of the curves are similar.

Similar results were obtained for a wall with carbon armour. The initial photon-induced peak is much smaller since the photon energy deposition goes deeper inside the carbon. Also, the maximum temperature is <2000°C with an associated sublimation loss of less than 1 μm per year.

In these calculations the energy deposition in the W armour was first calculated for a one-dimensional slab geometry based on photon attenuation calculations (including photo-electric and Compton scattering effects), and on ion energy deposition (including both electronic and nuclear stopping powers). The photon calculations were performed using the methodology described in [27]. An interactive program based on these calculations can be found at http://aries.ucsd.edu/LIB/PROPS/PHOTON/. The ion stopping was calculated using an interactive programme called SRIM (Stopping and Range of Ions in Materials), which may be found at http://www.srim.org/. The underlying physics is discussed in [28]. The calculation procedure included the time of flight spreading of the photon and ion energy deposition [29]. The thermal analysis was then carried out using a one-dimensional model including melting and evaporation [29]. Temperature-dependent properties were utilized for both C and W.

The BUCKY code [21] was used to explore the options for the case of the 400 MJ target. In this case, the chamber must be filled with Xe gas. To establish the low-density, high-temperature conditions of the Xe at the time the ions transit the chamber, the opacity of the Xe was determined using IONMIX [30], a collisional radiative equilibrium screened

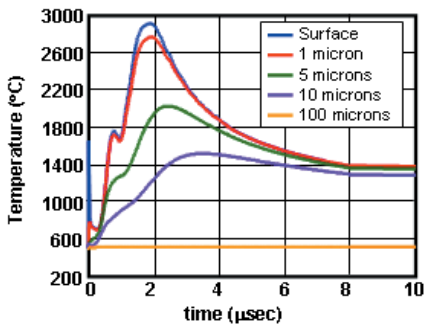

Figure 13. Temperature profiles of first wall in an IFE chamber, 154 target, tungsten wall.

Table 2. Summary of exposures of candidate first wall materials.

	Material	BUCKY predicted ablation threshold (J cm^{-3})	Analytic predicted ablation threshold (J cm^{-3})	Measured ablation threshold (J cm^{-3})	Measured roughening threshold (J cm^{-3})	Predicted threat to wall: 154 MJ target (J cm^{-3})	Predicted threat to wall: 400 MJ target (J cm^{-3})
X-rays (10 ns exposure)	Poco graphite	4.25	3.3	>8	<8 grain removal	0.40	1.20
	Tungsten (pure)	3.5–4.0	2.4	2.3–19	2.3		
	Tungsten + 25%Re			19	2.3		
	Tungsten + La			19	>2.3		
IONS (~100 ns exposure)	Poco graphite	3.2	1.8	2.5–3.0	<1	8.5	21.1
	Pyrolitic graphite	1.6–2.5	1.2–3.0	3.0–4.0	2.5		
	Tungsten (pure)	6	5.1	6	1.25		
	Tungsten + 25% Re			6	3.5	(1.82)	(4.54)

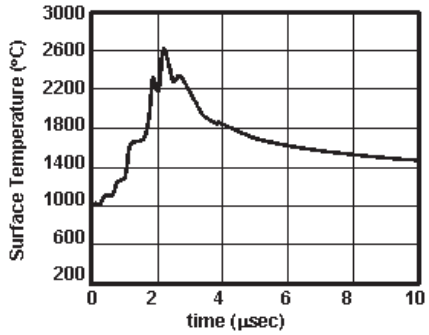

Figure 14. Wall surface temperature for a 8.25 m radius graphite chamber and the 400 MJ target.

hydrogenic model that interpolates between the low-density, high-temperature coronal equilibrium and the high-density, low-temperature Saha equilibrium. The wall is assumed to survive if the sublimation is less than one monolayer per shot. For a 6.5 m radius graphite chamber starting at 1000°C, the minimum Xe density required to avoid wall ablation is 80 mTorr, which is incompatible with target tracking as pointed out above. Increasing the chamber radius to 8.25 m reduces the threat to the wall sufficiently such that sublimation is avoided using 25 mTorr of Xe. Under these pressure and wall temperature conditions the target will require an outer layer of insulating foam to survive. Figure 14 displays the wall surface temperature evolution for a 8.25 m radius graphite chamber.

Both of these design window studies illuminate a few key points:

1. The photon energy deposition is very fast and creates an instantaneous temperature rise (for example, 1150°C in the case of the 154 MJ target with tungsten armour). The wall temperature starts to drop, and then peaks several microseconds later after the ions arrive.
2. With the 154 MJ target and tungsten wall chamber, the temperature stays under 3000°C for a 6.25 m chamber without any protective gas. This is below the W melting point limit (3410°C).
3. Similar arguments apply to the high-yield target and graphite wall. The temperature peaks under 2700°C for a 8.25 m chamber with 25 mTorr Xe, which is well below the temperature for significant sublimation.
4. In both cases the 'action' takes place in a very thin region ($<10\,\mu$m) from the surface. This gives the option to separate the functions of the first wall into two components: a thin armour, which is resistant to the target emissions, and an underlying substrate to provide the supporting structure and interface with the blanket. (Note that the blanket effectively sees steady-state conditions.)

5.1.5. Materials response: long-term behaviour. While the identification of chamber operating windows is a major step, long-term material behaviour is an issue, in particular tritium retention for carbon and helium retention for tungsten. It is anticipated that 0.1–2 MeV He, D, T, and H ions will penetrate several microns into the chamber wall. With carbon, the main concern is the build-up in tritium inventory due to co-deposition in colder regions. Additional concerns are dimensional stability, thermal conductivity following neutron irradiation, and physical and chemical sputtering. Good dimensional stability and thermal conductivity have recently been demonstrated for a high-quality three-dimensional composite irradiated at 800°C. Studies to higher, IFE relevant, temperatures (including tritium retention) are planned. In addition, safety studies carried out by two different groups suggest that oxidation due to a sudden ingress of air is not an issue with graphite-based first wall systems.

The main issue with tungsten is helium retention: the 3.45 MeV alpha particles embed themselves in the tungsten and, because of the extremely low mobility of helium, coalesce into bubbles that eventually cause the material to fracture. For example, for the anticipated fluence of 2×10^{18} He m^{-2} s^{-1}, it is estimated that this process will remove about 2 cm yr^{-1} from the wall. This is unacceptable, as the initial tungsten armour would be less than a few millimetres thick. We are addressing this issue with a multi-pronged approach:

1. The unacceptable removal rate is based on the assumption of limited helium mobility in tungsten. While this is documented at temperatures below 800°C [31], the behaviour at the elevated temperature of an IFE wall is unknown (note from figure 13 that the surface of the wall gets to almost 3000°C). Accordingly, experiments were performed to determine the diffusion of helium at IFE relevant temperatures. In these experiments, tungsten was irradiated at ∼1000°C and cyclically heated to 2000°C. Nuclear reaction analysis was used to determine the fate of the implanted helium. The results showed the amount of helium retained can be reduced by a factor of 2 or more. This work is preliminary and more experimental verification is needed—for example, the effects of neutron irradiation on helium mobility need to be evaluated.
2. In addition to these experimental results, preliminary modelling has shown the bubble formation may be not be a problem in an IFE system. This is because the ions produced by the target have a wide spectrum of energies, and thus the helium will be driven to a range of depths into the first wall, rather than into just one location. The predicted exfoliation, or loss, rate from the first wall would be an acceptable 0.078 cm per year. This result needs to be explored further and appropriate experiments conducted.
3. We are exploring the use of engineered materials such as tungsten fibres or nano-deposited tungsten. The idea is to provide a very short migration path for the helium to be transported back to the chamber. This can be accomplished by having the structure smaller than the helium mean free path, which is estimated to be of the order of a few tenths of microns. This material will also alleviate the roughening due to repetitive thermo-mechanical stresses, if that turns out to be an important factor.

5.2. Chamber dynamics

In a rep-rated laser-fusion facility, the pulse repetition rate is limited by the time it takes for the chamber environment to return to a sufficiently quiescent and clean low-pressure state to allow a second shot to be initiated. Laser propagation, beam quality on the target, and target injection and tracking will

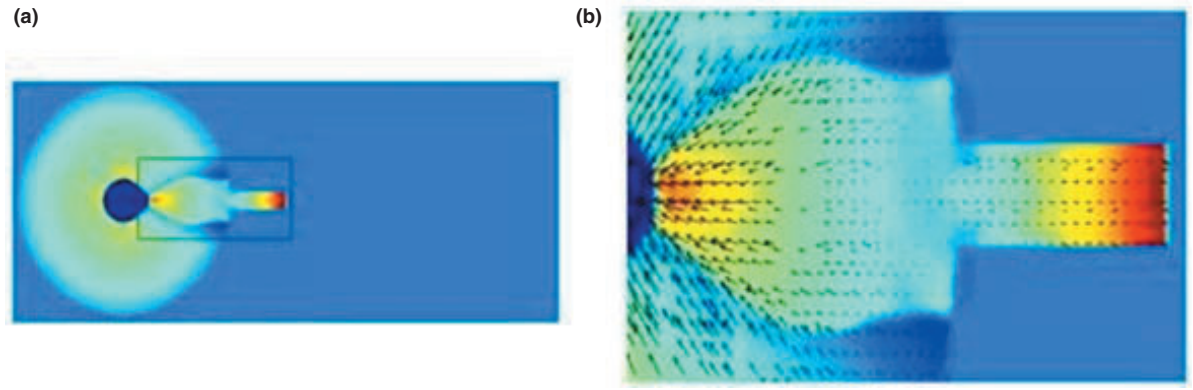

Figure 15. Conditions in the chamber 1.6 ms after the target blast. (*a*) Pressure and (*b*) velocity distribution. Pressure is the highest in the red zones (∼4 kPa) and lowest in the dark blue zones (∼300 Pa) and at intermediate values in the yellow zones (∼800 Pa). The blast has been reflected (once) from the chamber wall. A pressure wave is travelling in the laser beam channel toward the final optics.

all be affected by the chamber conditions (number density, temperature, mix of chamber constituents, and turbulence).

The physical phenomena occur on different timescales. In the first few microseconds, the x-ray burst and ions from the fireball traverse the chamber, and deposit their energy into the chamber constituents and onto the chamber wall. The chamber environment then evolves on a hydrodynamics timescale until a new equilibrium condition is achieved. This is expected to take 100–200 ms. To understand the chamber evolution and dynamic over this 'longer' timescale, a new simulation code, SPARTAN, has been developed.

SPARTAN solves the two-dimensional transient compressible Navier–Stokes equations. It uses split Godunov integrator in the CGF from [32, 33] that is second-order accurate in regions of smooth flow in order to capture the shocks with a minimum of numerical dissipation and overshoot. Several features have been included to make the code suitable for IFE applications:

1. In order to preserve the second-order accuracy of numerical algorithm, calculations are performed on a rectangular logical mesh. Arbitrary chamber geometry (e.g. inclusion of the laser beam ports) is handled by using an embedded boundary algorithm [34] that is also second-order accurate.
2. Viscous terms are added to the split Godunov integrator as viscosity plays an important role on this long timescale. The viscous interaction between the fluid and the embedded boundary was tested on the models of channel flow and lid driven flow in a square cavity. The channel direction was oriented at an arbitrary angle with respect to the mesh.
3. During the timescale of interest (100–200 ms or longer), the shock waves from the blast traverse the chamber many times. Large-scale pressure disturbances are set up that would require excessive computational time if a single homogeneous grid was used. As a result, an Adaptive Mesh Refinement Algorithm, AMR [35], has been employed. The integration of this algorithm into the code was done in collaboration with scientists at Lawrence Berkley National Laboratory [36]. The code can handle the strong shock waves in a computationally efficient manner, with fine grid surrounding the shock and coarse grid placed where the gradients of dependent variables are low.

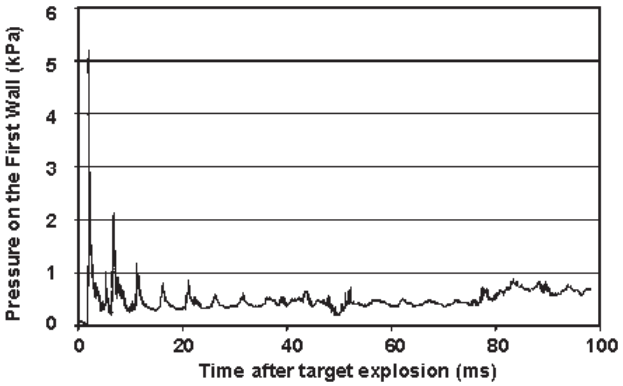

Figure 16. Pressure on the chamber wall as a function of time after target explosion. Initial peaks represent incidence of pressure waves on the chamber wall.

The code has been tested in simple geometries with both zero and small perturbation initial conditions. Some examples of the computational capabilities of the SPARTAN code are shown below. Figure 15 shows the pressure and velocity distribution in a cylindrical IFE chamber 1.6 ms after the blast. The chamber is 6.5 m in diameter and filled with Xe. One laser beam channel is included. The initial conditions for density, pressure, velocity, and energy of Xe gas are taken from the BUCKY [21] code after the temperature of the gas has fallen below 1 eV and radiation has become negligible. At the time shown in the figure, the blast wave has bounced from the chamber wall and is converging back towards the chamber centre. A pressure wave is travelling in the beam port towards final optics. Figure 16 shows the density distribution around the entrance of the laser beam channel at this time. The multi-dimensional nature of phenomena is clearly shown in these figures.

The code is currently investigating chamber conditions (pressure, velocity, density variations) 100–200 ms following the target blast. Non-uniformities have strong impact on target injection in the chamber and laser propagation. The code is also being used to study convection in the chamber, due to both off-centre target blasts and gravity, and to model the

impact of pressure waves on the final optics. Among planned improvements is the ability to handle multi-species transport. Of particular interest is the transport of dust in the beam tube channels.

6. Final optics

The final optics steer the laser beams to the target centre. They are the only optic to lie in the direct line of sight of the target. Their development represents the biggest challenge in the optical train, as they must not only have the high laser damage thresholds required of the other optics, they must also be resistant to the target emissions. The other optics will also require development, as their size, and hence to some extent the size of the system, will depend on their resistance to laser damage. But due to the greater challenges, resources have been concentrated on developing the final optic for now.

6.1. Grazing incidence metal mirror

The front-runner final optic concept is a grazing incidence metal mirror (GIMM). This was proposed over a decade ago in response to concerns over radiation damage to multi-layer dielectric mirrors [37]. The decision to develop the GIMM is based on its potential robustness, its ability to withstand some uniform erosion, and its applicability to both KrF and DPPSL wavelengths (241 nm and 351 nm, respectively). The final optic would consist of a pure aluminium surface bonded to a cooled, neutron transparent substrate [38]. Operation at a shallow angle ($\sim$85°) gives three advantages: reduced absorption for s-polarized light, lower average fluence on the surface due to the large footprint of the beam, and higher reflectivity. Experiments have established that, at least in small laser spot sizes, the aluminium mirror is both highly reflective (>98%) and can exceed the required laser damage threshold of 5 J cm^{-2}.

Laser damage is one of the most serious concerns for grazing-incidence mirrors. If the mirror operates at fluences beyond the normal incidence damage threshold, then minor defects may result in localized heating which causes further damage. The presence of contaminants, which could propagate from the chamber up the beamlines, might exacerbate this by creating a source term for localized defects. Therefore, initial testing has been focused on the basic stability of metal surfaces during long-term exposure. Aluminium is currently the preferred material due to its high reflectivity for UV wavelengths and the relatively large industrial database. Specifications for the damage threshold of commercially available Al-coated mirrors typically call for 20 mJ cm^{-2} of absorbed energy. With the reduced absorption and increased footprint of a grazing-incidence mirror, this should translate into a damage threshold of roughly 20 J cm^{-2} measured across the incident beam. We have set the goal laser fluence for the GIMM at 5 J cm^{-2} normal to the beam. This implies $\sim$400 m^2 of total mirror surface area for a 2 MJ laser.

The data were acquired using pure diamond-turned Al and a 2 J, 10 ns frequency-doubled Nd : YAG laser ($\lambda = 532$ nm). For these specimens, a natural density, 20–30 μm thick oxide coating is present. The results are shown in figure 17. The results confirm survival up to 10^4 shots for fluences well above

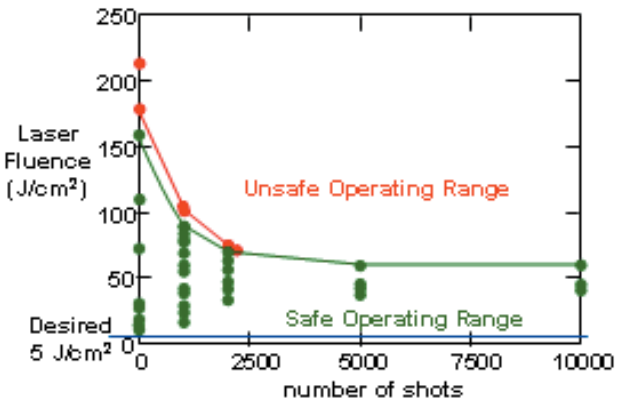

Figure 17. Laser-induced damage threshold (fluence is measured normal to the beam).

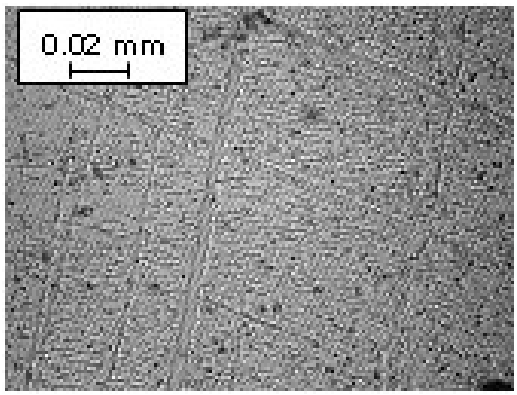

Figure 18. Morphology of thermo-mechanical damage to the surface.

20 J cm^{-2} [39]. Preliminary exposures at fusion-relevant UV wavelengths have shown that the damage threshold is lower, but still above the required 5 J cm^{-2}. The damage threshold, however, is highly dependent on the sample purity and the environment.

The morphology of damage in pure Al appears to be primarily thermo-mechanical in nature. Figure 18 shows a micrograph of the surface near a catastrophic damage site following 10^4 shots. Several types of roughness are evident. Large channels, thought to be the result of internal slip bands that propagate to the surface, appear in somewhat random fashion. Smaller elongated 'notches' appear in an orientation that corresponds with the direction of light propagation. These notches represent a rippling of the surface in a direction that does not affect the angle of incidence. Apparently, ripples aligned so as to produce a more normal angle of incidence to the beam are less likely to persist. The fine lines oriented at $\sim$45° are machining grooves resulting from diamond turning.

Since power plant optics are expected to be fabricated using thin coatings on a low-activation substrate, data on solid Al surfaces provide only a baseline for future testing of coated mirrors. Industrial collaborators recently have been engaged to fabricate coated optics. Their objectives are to demonstrate acceptable adhesion and damage threshold and to demonstrate the feasibility and optical characteristics of environmental protective surface coatings.

Table 3. Final optic threats.

Threat	Target emission (MJ shot)	Final optic
X-rays	5.6	0.11 J cm^{-2}
Neutrons	280	19.6 krad s^{-1}; 0.36 MW m^{-2}; 9.7×10^{12} n cm^{-2} s^{-1} (14 MeV)
γ-rays	$\ll$1	3.2 krad s^{-1}
Ionic debris	110	2.2 J cm^{-2} per shot; 0.15 MW m^{-2}

Multi-layer Fresnel, Kirchhoff scattering and ray-tracing analyses have been performed in order to better understand the optical characteristics of ideal and defected mirrors [40]. For example, a thin carbon coating on an oxidized Al mirror is harmful compared to a less absorptive water contaminant. Further studies are needed to fully characterize the effect of contaminants and their maximum allowable size and density, to demonstrate acceptable performance of prototypic coated substrates, to explore the effect of target emissions, and to scale up and integrate the final optic into integrated research facilities.

In addition to laser damage, the final optic is subjected to neutrons, x-rays, gamma rays and charged particles. Table 3 summarizes these threats at the final optic location, which is anticipated to be 20–30 m from the target chamber centre [23]. The threats assume no fill gas in the chamber. While the threats on the optic are reduced compared to that on the chamber walls at 6.5 m, these must still be addressed in view of the stringent beam quality requirements for target implosion. Our plan is to assess the effects of these threats on the optic. If they are found to be serious, we will then pursue mitigation techniques such as fast shutters, magnetic deflection, etc.

6.2. Transmissive optics

We have also investigated transmissive optics. The key issue is production of colour centres, which are induced by either neutrons or gammas, and which lead to optical absorption at the laser wavelength. The work has concentrated on SiO_2. Heating a SiO_2 optic allows the defect concentration to saturate at acceptable levels, at least at the DPSSL wavelength of 351 nm. For example, a 0.5 mm thick Fresnel lens operated at a temperature of 300°C is expected to have a laser absorption of $<$5% [41]. This is the equilibrium temperature the optic would reach (due to heating by laser and neutron absorption) if it was placed at a stand-off distance of 20 m. The defect population may be reduced further (with a corresponding reduction in optical absorption) by deliberately operating the optic at a higher temperature and taking advantage of thermal annealing. Figure 19 shows the laser absorption as a function of operating temperature of the final optic. For operation at 500°C, for example, the optical absorption falls to ∼0.6%. The power required to heat the optics to 500°C is of the order of 5 MW, which is more than compensated by the savings in required input power to the lasers.

The absorption is still too high at the KrF wavelength of 248 nm. This, plus the issues in fielding a thin, large area optic, has led us to give more attention to the GIMMs.

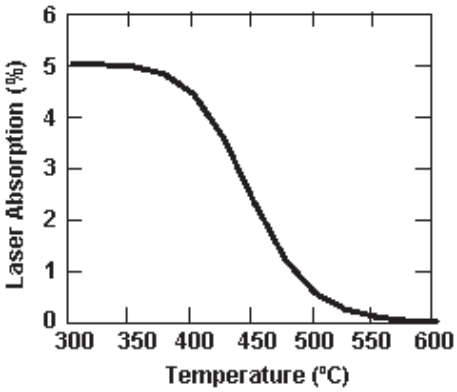

Figure 19. Heating the SiO_2 final optic to 500°C would reduce optical absorption at 351 nm to ∼0.6%.

7. Target fabrication

As discussed in section 2, the high gain target designs have a low density foam shell that has been overcoated with a thin layer of solid CH. An advanced divinyl benzene foam system was developed for this. This material was chosen because it has relatively high strength, it has no oxygen (which may be important for target physics), it can be made into IFE size shells by microencapsulation, and the overcoat can be chemically applied during the shell formation phase. Both of the latter are suited to mass production. Up to 300 shells, with proper diameter, density, and wall thickness, have been produced in a single batch (see figure 20). Methods to make target quality shells with the precise concentricity, reproducibility, and overcoating are being developed. In some target designs, the target is overcoated with a thin high-Z layer. A co-sputtering technique has been developed to apply an Au–Pd alloy coating to the outside of the target. Measurements show this Au–Pd alloy meets the requirements for DT permeation times (almost as good as pure Pd), and has high IR reflectivity (almost as good as pure gold) to help the target survive as it traverses the hot chamber. As discussed in section 2, target modelling shows this alloy does not compromise the gain.

A high gain target will require a smooth surface (less than 1.4 μm RMS) on the inner surface of the DT ice layer. Three advances have been made in this area:

1. Ultra smooth, DT ice layers have been made by growing the DT ice on a foam base. This arrangement replicates the current fusion energy target designs. A toroidal geometry was used in these experiments. The liquid DT was wicked into a low-density plastic foam, frozen at 19.7 K, and then slowly cooled to equilibrate at 19.25 K. The observed integrated (modes 4–256) variation in the DT ice surface finish was less than 0.6 μm, or more than two times better than what has been achieved without a foam underlay.
2. As the temperature is lowered, the smoothness of the DT ice layer grown over a foam layer suffered minimal degradation. For example, at temperatures just below 16 K (the limit of the equipment) the surface roughness increased by less than a factor of 2. This is comparable to the surface finish observed with a DT ice layer grown without foam *at the triple point*. This lack of layer

degradation is in contrast to DT layers grown without foam, in which the smoothness degrades catastrophically as the temperature is lowered.

3. A batch process layering technique is under development that is based on a fluidized bed technology. Experiments with a room temperature surrogate (oxalic acid) and an external infrared heat source (to mimic the natural heat from the tritium decay) have demonstrated the feasibility of this approach.

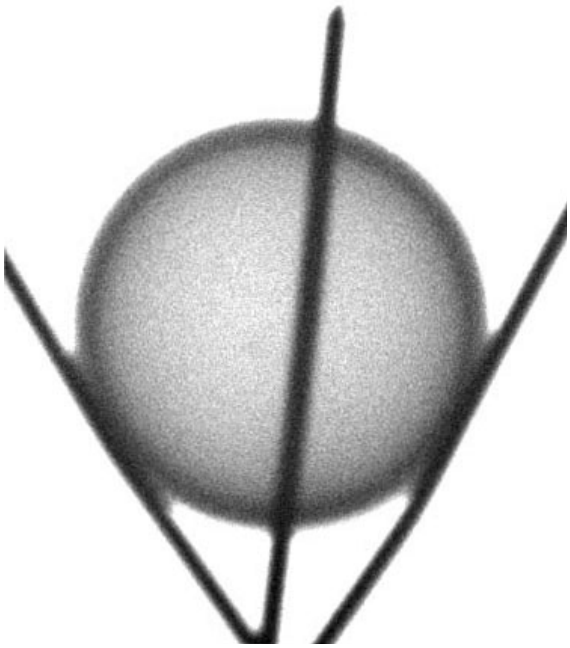

Figure 20. X-ray radiograph of a polymerized divinyl benzene foam shell. Shell is 4 mm diameter, has a wall of 300 μm thickness, and a density of 100 mg cc^{-1}.

Models have been developed to understand and guide the target production process. Using models of the material responses during the permeation filling step, the total tritium inventory in a laser fusion power plant could be under 300 g [42]. This is below the normally acceptable value of 1 kg. An analysis has been performed for estimating the cost for fabricating the direct drive targets discussed in section 2. This analysis was based on a chemical engineering analysis of all the process steps and assuming a commercial process plant environment. A conceptual plant is shown in figure 21. The analysis includes process flows, mass–energy balances, plant utilities, raw materials, quality control, waste handling and recycle, capital equipment cost amortization, and staffing requirements. The results give an estimated cost of producing a direct drive target of about 16.6 cents each. This is well under the 25 cents each called for by power plant studies [24], and resolves a major technical feasibility issue of Laser Fusion Energy.

8. Target injection

The two key issues with target injection are accuracy and target survival. In a power plant the target must be delivered to the chamber centre, to a precisely predicted target location at a repetition rate of 5 Hz. Target placement must be within $\pm$5 mm of a specified point at the target chamber centre. Target tracking must be accurate enough to enable precise alignment of the driver beams with the actual target position. Direct drive targets will require alignment of the centreline of the driver beams with the centreline of the target to less than about $\pm$0.02 mm. Target position prediction must be accomplished early enough to allow time for beam steering.

A system to study injection and tracking has been completed and is undergoing tests (see figure 22). This injector is designed to accelerate any target, be it of indirect

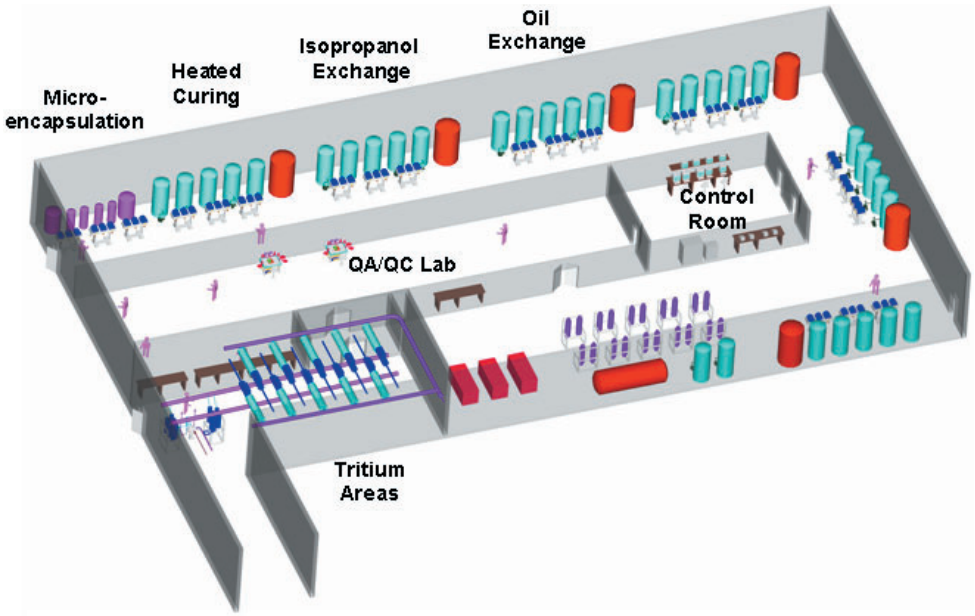

Figure 21. Preliminary plant layout for fabrication of high-gain, direct drive targets. Plant parameters are (*a*) 500 000 targets per day, (*b*) targets spend 2–3 weeks on the assembly line, (*c*) installed capital cost: \$97M, (*d*) annual operating cost: \$19M, and (*e*) estimated cost per target: 16.6 cents. Cost does not include tritium recovery, as per costing allocation in [24].

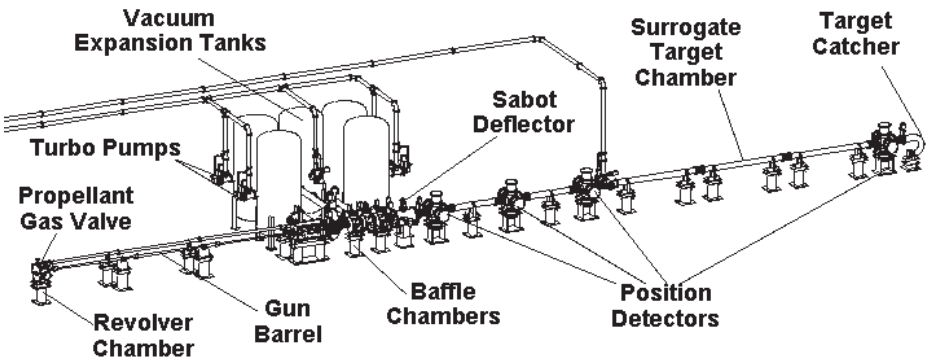

Figure 22. Drawing of target injection and tracking system.

or direct drive. For the direct drive targets, the concept of a separable sabot to protect the target during acceleration has been demonstrated. We are also performing experiments to measure the mechanical properties of frozen DT to predict the response of the target during the high g-loading of injection. Equipment is being constructed to develop and demonstrate accurate placement and precise tracking of targets during the injection [43].

Target survival, or how fast the target warms up on its way to the chamber centre, is one of the key factors that determine the chamber operating window described in section 5.1 (figures 13 and 14). The target heats up due to radiation from the wall and energy exchange with the gas [44]. The heat flux due to radiation ranges from 0.2 W cm^{-2} at 1000 K to 1.2 W cm^{-2} at 1500 K. The heat flux due to the gas is more complicated, as it depends on the target injection velocity, the gas condensation coefficient, and the gas temperature. Eventually the gas temperature will be determined by the chamber dynamics code, but for now we take a range of values. For example, for a gas pressure of 25 mTorr, a gas temperature of 2000 K, a target injected at 400 ms^{-1}, and a condensation coefficient of 1, the heat flux on the target due to the gas is 3 W cm^{-2}. In general, the total heat flux on the target is predicted to range from 1 to 10 W cm^{-2}. Starting at a lower target temperature helps in increasing the total allowable heat flux. Assuming the target velocity above, for every degree K that the target is cooled below the triple point temperature, an additional 0.34 W cm^{-2} can be absorbed. This is why the ability to produce smooth layers at the coldest possible temperatures is so important.

The maximum allowable temperature limit is open to question. One possible limit is when the internal stresses due to thermal expansion (non-uniform heating of the DT ice from the outside) are greater than the yield stress. Thus, this limit is reached when the inner ice surface smoothness is degraded by deformation. A more likely limit is when the outside layer of DT exceeds the triple point, 19.79 K, at which point the smooth outer surface of the solid cryogenic ice layer transitions to liquid or gas. If the outer surface of the DT goes to a pure uniform liquid that does not affect the areal mass distribution, the effect on the target implosion will be minimal. Hence, the allowable temperature limit could be much higher. However, if the DT goes to a liquid/gas state, bubbles may form at the seal coat/DT boundary which would affect the areal mass distribution and which could adversely impact the target stability. Whether the phase change is to liquid or to gas is governed by the local pressure at the interface of the outer DT surface and the hydrocarbon layer just above it. This is a very complex phenomenon. In the absence of any hard data or trustworthy models, the upper limit has been taken as the DT triple point as described above.

How fast the outside surface of the DT reaches the triple point depends on how fast the incident heat can be transported away from the DT surface. As the situation is dynamic, the calculations are carried out over the target time of flight. All the calculations are based on the available data on the properties of DT and plastic at cryogenic temperatures. Accurate and representative material property data are required for this modelling. Material property measurements, modelling of these effects, and experiments to measure the thermal response time of DT and DT + foam, are underway to provide a more accurate prediction of the target thermal response.

9. Development of laser fusion energy

We propose to develop a viable fusion energy source in three distinct phases. Specific critical issues must be resolved before advancing from one phase to the next. Each phase represents increasing confidence, decreasing technical risk, and increasing cost. In all phases the various components will be developed in concert with one another to ensure we are developing laser fusion energy as an integrated system. We are currently in Phase I, which will develop the critical science and technologies. Phase II would develop, test, and integrate full-size components. This will include a full-scale, power plant sized laser beam line and a separate facility to demonstrate repetitive injection of fusion quality targets into an IFE chamber environment. Phase III is the construction and utilization of a single flexible Engineering Test Facility (ETF). This ETF would serve several functions including: (1) optimization of the laser–target and target–chamber interactions; (2) development of materials and components; and (3) demonstration of substantial net electricity generation at a high duty factor from fusion. We believe that we could be prepared technically to start construction of the ETF facility within 10–12 years, with the basic issues resolved well before 2030. The knowledge base with ETF research should be sufficient that follow-on fusion facilities could be commercially attractive investments.

Table 4. Summary of progress and outstanding issues for laser fusion energy.

Target design	
Progress	1. Produced family of target designs, using benchmarked codes, that have one-dimensional gains ∼160 (fusion energy needs/gain >100)
	2. Newer two-dimensional calculations produced similar gains
	3. Produced a family of target designs that can meet the other needs for IFE: fabrication, injection, tritium inventory
Issues	1. Verify a robust family of target designs, using two-dimensional and three-dimensional modelling
	2. Benchmark designs with experiments
Lasers (KrF)	
Progress	1. Demonstrated repetitive first light
	2. Demonstrated pulsed power switch to meet efficiency and durability
	3. Demonstrated required efficiency in main components
Issues	1. Durability: hibachi foil and amplifier window
Lasers (DPPSL)	
Progress	1. Demonstrated repetitive first light in new type of laser architecture
	2. Demonstrated gas cooled amplifier head and high peak power diodes
Issues	1. Cost of diodes, development of large size crystals
Chambers	
Progress	1. Established chamber operating windows for wide range of targets
	2. Developed chamber clearing code, 'SPARTAN'
	3. Evaluated first wall materials response to x-rays and ions
Issues	1. Long-term materials: He bubble induced exfoliation for W, and T_2 retention for carbon
	2. Blanket and underlying, fusion neutron resistant-structures
Final optics	
Progress	1. Demonstrated GIMM meets reflectivity and laser damage requirements
Issues	1. Bonding of reflective layer to neutron transparent substrate
	2. Develop final optics structure that is resistant to degradation from neutrons, x-rays, ions, and debris
Target Fabrication	
Progress	1. Modelling shows target cost ∼$0.16 each
	2. Demonstrated ultra-smooth DT ice layer grown over foam
	3. Made foam shells with proper dimensions and density
	4. Developed Au–Pd coating for both DT permeation and IR reflectivity
Issues	1. Develop mass production cryogenic layering technique
	2. Make foam shells that meet all IFE specifications
Target Injection	
Progress	1. Target injector completed
	2. Separable Sabot concept demonstrated
	3. Demonstrated sufficiently smooth DT ice layers at $t < 16$ K
Issues	1. Demonstrate sufficient accuracy in target tracking ($< +/- 20\,\mu$m)
	2. Target designs with enhanced thermal heat load resistance (e.g. foam layer outside target) to open parameter space for injection

10. Summary: progress and challenges in the development of laser fusion energy

Table 4 gives a capsule summary of the technical progress and the critical issues that must be resolved before proceeding to Phase II in the development of laser fusion energy.

Acknowledgments

Others have made contributions to the development of Laser Fusion as part of this programme, although their specific work was not cited in the manuscript. These researchers are from the following institutions:

Government Labs: Naval Research Laboratory, Lawrence Livermore National Laboratory, Los Alamos National Laboratory, Oak Ridge National Laboratory, Sandia National Laboratory, Princeton Plasma Physics Laboratory.

Industry: General Atomics, Titan-Pulse Sciences Division, Schafer Corp., Science Applications International Corp., Northrop-Grumman Corp, Coherent, Inc, Commonwealth Technology, Inc.

Universities: University of California, San Diego; University of Wisconsin; University of California, Los Angeles; University of Rochester Laboratory for Laser Energetics; and the Georgia Institute of Technology.

This work is sponsored by the US Department of Energy, NNSA/DP.

References

[1] Bodner S.E., Colombant D.G., Schmitt A.J. and Klapisch M. 2000 High gain direct drive target design for laser fusion *Phys. Plasmas* **7** 2298

[2] Colombant D. *et al* 2000 Effects of radiation on direct drive laser fusion targets *Phys. Plasmas* **7** 2046

[3] Bodner S.E., Colombant D.G., Schmitt A.J., Lehmberg R.H., Obenschain S.P. and Gardner J.H. 2000 New high gain target design for a laser fusion power plant *IAEA Technical Committee Meeting on Physics and Technology of Inertial Fusion Energy Targets and Chambers (Madrid, Spain, 7–9 June 2000)*

[4] Skupsky S. *et al* 2002 High-gain direct-drive target designs for the national ignition facility *Inertial Fusion Sciences and Applications 2001* ed K.A. Tanaka, D.D. Meyerhofer and J. Meyer-ter-Vehn (Paris: Elsevier) pp 240–5

[5] Goncharov V.N. *et al* 2001 Modeling hydrodynamic instabilities in inertial confinement fusion targets *Phys. Plasmas* **7** 5118

[6] Betti R. *et al* 2001 Hot spot dynamics and deceleration-phase Rayleigh–Taylor instability of imploding inertial confinement fusion capsules *Phys. Plasmas* **8** 5257

[7] Obenschain S.P. *et al* 2002 Effects of thin high-Z layers on the hydrodynamics of laser-accelerated plastic targets *Phys. Plasmas* **9** 2234

[8] Collins T.J.B. and Skupsky S. 2002 Imprint reduction using an intensity spike in OMEGA cryogenic targets *Phys. Plasmas* **9** 275

[9] Betti R. *et al* 1998 Growth rates of the ablative Rayleigh–Taylor instability in inertial confinment fusion *Phys. Plasmas* **5** 1446

[10] Haan S.W. 1989 Onset of nonlinear saturation for Rayleigh–Taylor growth in the presence of a full spectrum of modes *Phys. Rev.* A **39** 5812

[11] Sethian J.D., Friedman M., Giuliani J., Lehmberg R., Myers M., Obenschain S., Hegeler F. and Swanekamp S. 2002 Electra: a krypton fluoride laser for fusion energy *Inertial Fusion Sciences and Applications* ed K.A. Tanaka, D.D. Meyerhoffer and J. Meyer-ter-Vehn (Amsterdam: Elsevier) p 495

[12] Friedman M., Myers M., Swanekamp S.B., Chan Y., Sethian J.D. and Obenschain S. 2002 Suppressing the transit-time instability in large-area electron-beam diodes *Appl. Phy. Lett.* **81** 1597

[13] Orth C.D., Payne S.A. and Krupke W.F. 1996 A diode pumped solid state laser driver for inertial fusion energy *Nucl. Fusion* **36** 75

[14] Skidmore J.A., Freitas B.L., Crawford J., Satariano J., Utterback E., DiMercurio L., Cutter K. and Sutton S. 2000 Silicon monolithic microchannel-cooled laser diode array *Appl. Phys. Lett.* **77** 10

[15] Marshall C.D., Payne S.A., Smith L.K., Powell H.T., Krupke W.F. and Chai B.H.T. 1995 1.0047 μm $Yb : Sr_5(PO_4)_3F$ energy storage optical amplifier *Selected Topics in Quantum Electron.* **1** 67

[16] Bayramian A.J., Bibeau C., Schaffers K.I., Lawson J.K., Marshall C.D. and Payne S.A. 1999 Development of ytterbium doped $Sr_5(PO_4)_3F$ for the mercury laser project *OSA Trends in Optics and Photonics Series* ed M.M. Fejer, H. Injeyan and U. Keller vol 26 of OSA Proceedings Series (Washington, DC: Optical Society of America) pp 635–41

[17] Ebbers C.A., Kanz K. and Nakano H. 2002 A thermally compensated, deuterated KDP Q-switch for high average power lasers *Conference for Lasers and Electro Optics (Long Beach, CA, 19–24 May)* Paper CTuI6

[18] Waxer I.J., Kelly J.H., Rothenberg J., Babushkin A., Bibeau C., Bayramian A. and Payne S. 2002 Precision spectral sculpting for narrow-band amplification of broadband frequency-modulated pulses *Opt. Lett.* **27** 1427

[19] Schaffers K.I., Tassano J.B., Bayramian A.B. and Morris R.C. 2003 Growth of Yb : S-FAP [Yb^{3+}: $Sr_5(PO_4)_3F$] crystals for the mercury laser *J. Cryst Growth* **253** 297–306

[20] Zimmerman G.B. and Kruer W.L. 1975 Numerical simulation of laser-initiated fusion *Comments Plasma Phys.* **2** 51

[21] Peterson R.R., MacFarlane J.J. and Moses G.A. 1996 BUCKY-1—a 1-D radiation hydrodynamics code for simulating inertial confinement fusion high energy density plasmas *Fusion Technol.* **30** 783

[22] Raffray R., Federici G., Hassanein A. and Haynes D. 2002 Dynamic chamber armor behavior in IFE and MFE *Proc. Sixth Int. Symp. on Fusion Nuclear Technology (San Diego, CA 7–12 April)* (Amsterdam: Elsevier Science Ltd, pp 63–4

[23] Sviatoslavsky I.N. *et al* 1992 A KrF laser driven inertial confinement fusion reactor 'SOMBRERO' *Fusion Technol.* **21** 1470

[24] Meier W.R. and von Rosenberg Jr C.W. 1992 Economic modeling and parametric studies for SOMBRERO—a laser-driven IFE power plant *Fusion Technol.* **21** 1552

[25] McGeoch M.W. 1998 Radio-frequency-preionized xenon Z-pinch source for extreme ultraviolet lithography *Appl. Opt.* **37** 1651

[26] Stamper J.A., Lehecka T., Lehmberg R.H., Deniz A.V. and McLean E.A. The use of inert gases in KrF laser-driven ICF reactors *Nuc. Fusion* submitted for publication

[27] Berger M.J. and Hubbell J.H. 1987 XCOM: photon cross sections on a personal computer National Bureau of Standards, NBSIR 87–3597

[28] Bohr N. 1948 *Mat. Fys. Medd. Dan. Vid. Selsk.* **18**

[29] Raffray A.R., Haynes D. and Najmabadi F. 2003 IFE chamber walls: requirements, design options, and synergy with MFE plasma facing components *J. Nucl. Mater.* **313** 23

[30] MacFarlane J.J. 1989 *Comput. Phys. Commun.* **56** 259

[31] Wang W., Roth J., Lindig S. and Wu C.H. 1999 Blister formation of tungsten due to ion bombardment *J. Nucl. Mater.* **299** 124

[32] Colella P., Glaz H.M. and Ferguson R.E. 1997 Multifluid algorithms for eulerian finite difference methods CGF 1/31/1997

[33] Colella P. and Glaz H.M. 1985 Efficient solution algorithms for the Riemann problem for real gases *J. Comput. Phys.* **59** 264

[34] Modiano D. and Colella P. 2001 A higher order embedded boundary method for time dependent simulation of hyperbolic conservation laws *Proc. ASME 2000 Fluids Engineering Division Summer Meeting (Boston, MA, June 2000)* New York: American Society of Mechanical Engineers p 267

[35] Almgren A.S., Bell J.B., Colella P., Howell L.H. and Michael L. Welcome 1998 An adaptive projection method for the variable density incompressible Navier–Stokes equations *J. Comput. Phys.* **142** 1

[36] Day M. 2002 Lawrence Berkeley National Laboratory, private communications

[37] Bieri R.L. and Guinan M.W. 1991 Grazing incidence metal mirrors as the final elements in a laser driver for inertial confinement fusion *Fusion Technol.* **19** 673

[38] Ghoniem N.M. and El-Azab A. 1995 Thermomechanical design of the grazing incidence metal mirror of the prometheus-LIFE reactor *Fusion Eng Des* **29** 89

[39] Zaghloul M.R., Tillack M.S. and Mau T.K. 2002 Laser-induced damage of metal mirrors under long-term exposure at shallow angle of incidence *Proc. 19th IEEE/IPSS Symp. on Fusion Engineering (Atlantic City, NJ, 21–25 Jan. 2002)* (New York: IEEE) p 272

[40] Mau T.K., Tillack M.S. and Zaghloul M.R. 2002 Modeling of mirror surface damage effects on beam propagation in a laser-driven IFE power plant *Proc. 19th IEEE/IPSS Symp. on Fusion Engineering (Atlantic City, NJ, 21–25 Jan. 2002)* (New York: IEEE) p 118

[41] Latkowski J.F., Kubota A., Caturla M.J., Dixit S.N., Speth J.A. and Payne S.A. 2003 Fused silica final optics for inertial fusion energy: radiation studies and system-level analysis *Fusion Sci. Technol.* **43** 1565

[42] Schwendt M., Nobile A., Gobby P.L., Steckle W.P., Colombant D.G., Sethian J.D., Goodin D.T. and Besenbruch G.E. 2003 Tritium inventory of inertial fusion energy target fabrication facilities: effect of foam density and consideration of target yield of direct drive targets *Fusion Sci. Technol.* **43** 217

[43] Petzoldt R.W., Goodin D.T., Nikroo A., Stephens E., Siegel N., Alexander N.B., Raffray A.R., Mau T.K., Tillack M., Najmabadi F., Krasheninnikov S.I. and Gallix R. 2002 Direct drive target survival during injection in an inertial fusion energy power plant *Nucl. Fusion* **42** 1351

[44] Goodin D.T., Alexander N.B., Gibson C.R., Nobile A., Petzoldt R.W., Siegel N.P. and Thompson L. 2001 Developing target injection and tracking for inertial fusion energy power plants *Nucl. Fusion* **41** 527